J Solid State Electrochem (2008) 12:841–849
DOI 10.1007/s10008-007-0444-8

ORIGINAL PAPER

Design of nanostructured ceria-based solid electrolytes for development of IT-SOFC

Toshiyuki Mori · Richard Buchanan · Ding Rong Ou · Fei Ye · Tomoaki Kobayashi · Je-Deok Kim · Jin Zou · John Drennan

Received: 1 July 2007 / Revised: 28 September 2007 / Accepted: 2 October 2007 / Published online: 7 November 2007

Abstract A considerable interest has been shown in the application of doped ceria (CeO_2) compounds for "intermediate" (300–500 °C) temperature operation of solid oxide fuel cells. The microdomains with ordered structure of oxygen vacancy were observed in the microstructure of the M-doped CeO_2-sintered bodies (where M: Gd, Y, and Dy). We have previously shown that the conductivity of doped CeO_2-sintered bodies was lower when the sintered body contained large microdomains within grains. As a consequence of this observation, we have examined the grain size dependence and dopant content on conductivity in specimens where we adjust the microdomain size and a degree of oxygen vacancy ordering in the microdomains by controlling the microstructure. The microdomain size control in Dy-doped CeO_2 specimens was obtained by combining pulsed electric current sintering and conventional sintering. Using these techniques, we were able to improve the conductivity in Dy-doped CeO_2 specimens to a point where it became comparable to that of the more conventional Gd-doped CeO_2 specimens. It is concluded that by combining ultimate high-resolution analysis of these nanostructures with the adjusting processing route design, it is possible to further develop these materials in CeO_2-doped fuel cell application.

Keywords Doped CeO_2 solid electrolyte · Microdomain · Oxygen vacancy ordering · Grain size dependence of conductivity · Solid oxide fuel cell

This paper contributes to ICMAT 2007, Symposium K: Nanostructured and Bulk materials for Electrochemical Power Sources.

T. Mori (✉) · R. Buchanan · D. R. Ou · F. Ye · T. Kobayashi · J.-D. Kim
Nano-ionics Materials Group, Fuel Cell Materials Center,
National Institute for Materials Science,
1-1 Namiki,
Tsukuba, Ibaraki 305-0044, Japan
e-mail: MORI.Toshiyuki@nims.go.jp

J. Zou · J. Drennan
Center for Microscopy and Microanalysis,
The University of Queensland,
St. Lucia,
Brisbane, Queensland 4072, Australia

Introduction

Oxide ion conductors are used in a variety of oxygen sensors [1–3], solid oxide electrochemical cells [4–6], and solid oxide fuel cells (SOFCs) [7–9]. Of these applications, SOFCs are being especially developed as a clean and efficient power source for generating electricity from a variety of fuels. Doped CeO_2 compounds such as Gd-doped CeO_2 [10–12] and Sm-doped CeO_2 [13–16] are now under active investigation for application as electrolytes in what are classed "intermediate" (300–500 °C) temperature operating SOFCs. These electrolytes show high oxide ion conductivity at high oxygen partial pressures. However, at low oxygen partial pressures, associated with anodic conditions, these materials are partially reduced and develop electronic conductivity during operation of the fuel cell. To overcome this problem and improve the conductivity for "intermediate" temperature operation of SOFCs (IT-SOFCs), the influence of the microstructural feature at the atomic scale in doped CeO_2 systems on the conducting properties should be taken into account. Concentrating on the microstructure at high resolution will ultimately provide information on the conduction pathway in nanostructured solid electrolytes. A consequence of this approach is that a new design paradigm is required for a development of high-quality doped CeO_2 solid electrolytes in IT-SOFCs.

To design the microstructure of doped CeO_2 solid electrolytes, the authors have observed the microstructural features at atomic scale of various doped CeO_2-based oxides, such as Sm^{3+} [16–18], La^{3+} [17, 19], Y^{3+} [20–22], Dy^{3+} [23], Gd^{3+} [24], Yb^{3+} [25], and Tb^{3+} [26–28], doped ceria-sintered bodies using transmission electron microscopy (TEM). In these doped CeO_2-sintered bodies, the microdomains with ordered structure of oxygen vacancy have been observed using electron energy-loss spectroscopy (EELS) [29]. It has been demonstrated that the microdomains contribute to the decrease in the conductivity, and this is related to an associated increase in doping concentration. In addition, our previous detailed microanalysis work clarified a part of compositional and structural relationship that controls microdomain formation in these doped CeO_2-sintered bodies. However, this was a preliminary finding, and what is required is more detailed information on the relationship between microstructural features and electrolytic properties in these ceria-doped systems. This work delivers this information with a view to delivering a new design concept for an optimization of microstructure at the atomic scale to maximize the oxide ionic conductivity of doped CeO_2 solid electrolytes in IT-SOFCs. In the present work, the grain size dependence of conductivity of $Gd_xCe_{1-x}O_{2-x/2}$ (x=0.1, 0.15, 0.2, and 0.25) were systematically investigated. In addition, we compared those results with the results of Y-doped CeO_2 series [21] to discuss the difference of the grain size dependence of conducting properties between Y- and Gd-doped CeO_2-sintered bodies. To develop this new design concept, we also compared the conductivity of pulsed electric current sintering specimen with conventionally sintered specimens. Then, based on these comparisons, a new design concept for fabrication of nanostructured doped CeO_2 solid electrolytes is discussed.

Experimental

Synthesis of nanosize M-doped CeO_2 (M=Gd, Y, or Dy) powders

Starting materials used were $Ce(NO_3)_3{\cdot}6H_2O$ (99.99%, Kanto Chemical, Japan), $Gd(NO_3)_3{\cdot}6H_2O$ (99.95%, Kanto Chemical), dysprosium nitrate hexahydrate ($Dy(NO_3)_3{\cdot}6H_2O$; >99.95% pure, Wako Pure Chemical Industries, Ōsaka, Japan), $Y(NO_3)_3{\cdot}6H_2O$ (99.95%, Kanto Chemical), dysprosium nitrate hexahydrate ($Dy(NO_3)_3{\cdot}6H_2O$; >99.9% pure, Wako Pure Chemical Industries, Japan), and $(NH_4)_2CO_3$ (min 30% NH_3, Wako Pure Chemicals). These chemicals were used as received. For each composition, a mixed M/Ce (M=Gd, Y, and Dy) nitrate solution was prepared by adding the nitrates in the appropriate molar ratio of the composition of interest to make up a 300-ml solution with a total M^{3+} and Ce^{3+} concentration of 0.15 M. Dissolution was aided by stirring at 40 °C for ~30 min. The precipitant solution was 300 ml of 1.5 M $(NH_4)_2CO_3$, which was maintained at 70–75 °C during dissolution of the $(NH_4)_2CO_3$. In the carbonate precipitation reaction, the mixed nitrate solution was added dropwise (one to two drops per second) to the precipitant solution that was kept at 70–75 °C, with gentle stirring during the process. When all of the mixed nitrate solution was added, the reaction mixture was left to develop for 1 h at 70–75 °C with gentle stirring. After this development time, this mixture was filtered by suction filtration, and the precipitate was washed five times (three times with water, two times with ethanol). The precipitate was then blow dried for at least 48 h with flowing nitrogen at ambient temperature. Finally, the dried solid was crushed in an alumina mortar and pestle, sieved, and calcined in flowing oxygen for at least 2 h at a temperature between approximately 500 and 1,000 °C (depending on how fine or coarse a powder was needed to control the average grain size of sintered specimens).

Fabrication of sintered bodies

The nanosize powders were uniaxially pressed at 20 MPa to make compact bodies. After this, the compact bodies were pressed using cold isostatic pressing at 200–250 MPa. These compact bodies were then sintered in static air, heated at 5 °C/min to the desired temperature, and held isothermally for 6 h. Sintering temperatures were in the range 1,000 to 1,550 °C. In the combined process, a two-step sintering process was performed. The first step uses the pulsed electric current sintering (PECS), which is followed in the second step by conventional sintering (CS). For PECS, 2 g of the powders were placed into a 15-mm graphite-die and an electric current of 1,000 Å was applied under a pressure of 60 MPa. The heating rate was 500 °C/min. The sintering temperature ranged from 1,000 to 1,150 °C. To minimize the penetration of carbon from the graphite-die into the specimens, no holding time at the aforementioned sintering temperature was used. If the heating rate of PECS process was less than 500 °C/min, however, the sintered specimen became black. This indicates that the PECS specimen is reduced during the process by slow heating rate treatments. To further avoid reduction that might be caused by slow cooling the specimens, after the system reached the sintering temperature, the current was simply shut off at the temperature and the pressure was immediately released. After the PECS process, the specimens were sintered at the temperature ranging from 1,050 °C for 24 h in air. The specimens were oxidized and densified by this conventional sintering process after PECS process.

After cooling to ambient temperature, the bulk densities of sintered pellets were determined using the Archimedes method. The relative densities of the sintered pellets were calculated from the ratio between bulk density and the density calculated from X-ray diffraction data.

Microstructure analysis

The particle sizes in the synthesized powders and the grain sizes of the sintered bodies were observed using scanning electron microscopy (SEM). The average grain size in the sintered bodies was calculated using the linear intercept method measuring more than 300 grains recorded by SEM [30]. The microstructural features within the grain were investigated in detail using TEM. To prepare TEM specimens, small disks with a diameter of 3 mm were cut with an ultrasound cutter from the sintered samples. The disks were thinned to a thickness of ~70 μm by mechanical grinding and dimpled to a central thickness of ~30 μm; this was followed by ion beam thinning to produce a specimen thin enough for TEM observation. TEM observation was performed with gun voltages of 200 keV. High-resolution TEM was performed in JEOL JEM-2100F TEM. Selected area electron diffraction patterns (SAEDPs) of the specimens were obtained in JEOL JEM-2000EX TEM using an aperture size about 0.2 μm on the image. Energy-filtering TEM and EELS were conducted in a FEI Tecnai G^2 F30 TEM equipped with a Gatan imaging filtering system and operated at an accelerating voltage of 300 kV. The EELS spectra were acquired using collection aperture size of 2 mm, acquisition time of about 2−3 s, and an energy dispersion of 0.3 eV per channel. After calibration of the spectra, the background was removed using a power-law technique [31].

Conductivity measurement

For the electrical conductivity measurement, platinum electrodes were applied to both sides of the sintered bodies at 900 to 1,000 °C. The conducting properties in the sintered bodies were measured by direct current three-point measurements at 400 to 650 °C in air. The activation energy was calculated using the data of conductivity at the temperature ranging from 400 to 650 °C. For the evaluation of oxygen partial pressure (P_{O2}) dependence of conductivity, the additional conductivity measurements were carried out over a P_{O2} range of 1 to 10^{-21} atm. The atmospheres used were as follows (P_{O2} levels are shown in parentheses): oxygen (0.9–1 atm), air (0.2 atm), argon (10^{-3} atm), 10% H_2/He (10^{-21} atm), and wet 10%H_2/He (10^{-19} atm). Average equilibrium time at each P_{O2} level was 30 min. P_{O2} levels were measured using an external oxygen gas sensor operating at 800 °C that monitored the outlet gases. To minimize the condensation of moisture in the stainless gas line between the external oxygen gas sensor and furnace for conductivity measurement, the gas line is heated at 40 °C using a ribbon heater.

Results and discussion

The representative morphologies of calcined $Gd_{0.2}Ce_{0.8}O_{1.9}$ particles are shown in Fig. 1a and b. The calcined CeO_2

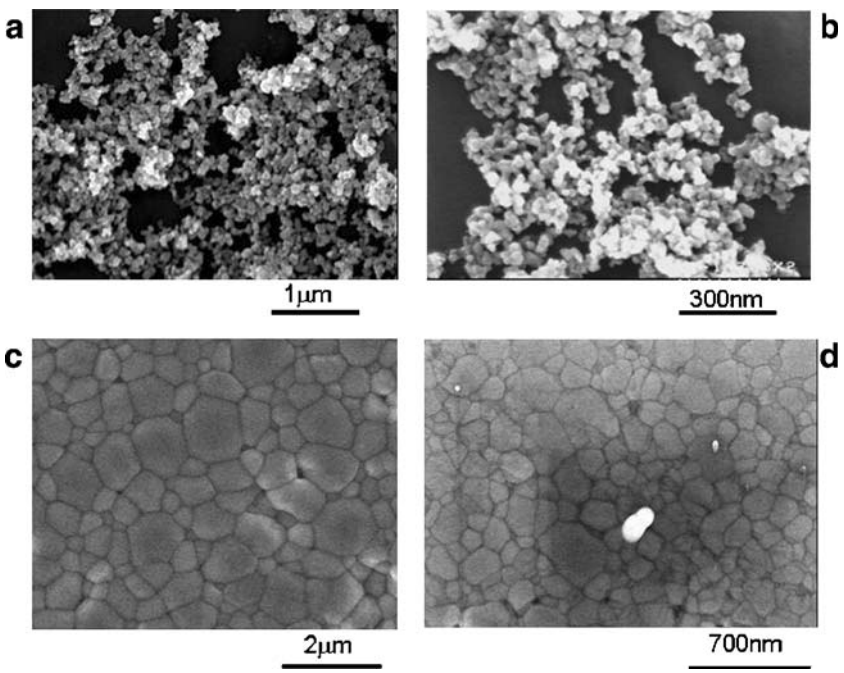

Fig. 1 SEM images of particle morphologies of calcined $Gd_{0.2}Ce_{0.8}O_{1.9}$ particles at high magnification (**a**), low magnification (**b**), and microstructures of $Gd_{0.2}Ce_{0.8}O_{1.9}$ specimens sintered at 1,450 (**c**) and 1,050 °C (**d**). Calcination temperature of powder=700 °C, sintering time of specimen=4 h

particles doped with Gd^{3+} were observed to be composed of uniformly sized, round, discrete particles. The average particle size of the powders was in the range of between 20 and 30 nm. This powder can be sintered to more than 95% of the theoretical density in the temperature range of 1,000 to 1,550 °C using conventional sintering. The morphology and average size of particles, which were doped with Y or Dy, showed similar characteristics of that previously described for Gd doping and, similarly, they could be sintered to more than 95% of theoretical density. SEM images of the microstructure of CS $Gd_{0.2}Ce_{0.8}O_{1.9}$-sintered bodies are shown in Fig. 1c and d. These figures clearly show that sintered specimens are dense with few pores. The grain size of specimen sintered at 1,450 °C was 1 to 2 μm; this is in contrast to a specimen with a small average grain size (330 nm) that was sintered to full density at 1,050 °C. This indicates that the average grain size of Gd-doped CeO_2-sintered bodies can be controlled within the range from several hundred nanometer levels to micrometer level using our prepared powders. This range of grain size can also be controlled in the dense CeO_2-sintered bodies doped with Y or Dy.

Figure 2 presents the relationship between conductivity and nanostructural features we have characterized in $Gd_xCe_{1-x}O_{2-x/2}$ (x=0.1, 0.15, 0.2, and 0.25) specimens sintered at 1,550 °C. The conductivity of Gd-doped CeO_2 electrolytes shows a maximum at the composition around x=0.15 in the $Gd_xCe_{1-x}O_{2-x/2}$ system. To conclude why the conductivity is optimized at this value of doping, in Gd-doped CeO_2, the crystal phases and associated nanostructural features in the sintered bodies were examined with a view to observing any correlations. The SAEDPs recorded from $Gd_{0.1}Ce_{0.9}O_{1.95}$- and $Gd_{0.25}Ce_{0.75}O_{1.875}$-sintered bodies have extra reflections associated with diffuse scattering, and this is in contrast to the X-ray diffraction profiles recorded from these sintered bodies, which indicate a simple fluorite phase. In addition, the intensity of extra reflection and diffuse scattering in SAEDP of $Gd_{0.25}Ce_{0.75}O_{1.875}$ is much stronger than that of $Gd_{0.1}Ce_{0.9}O_{1.95}$. This indicates that both specimens exhibit diffraction phenomenon consistent with the existence of microdomains representing some coherent ordered structure associated with oxygen vacancies. The average microdomain size in $Gd_{0.25}Ce_{0.75}O_{1.875}$ is larger than that observed in $Gd_{0.1}Ce_{0.9}O_{1.95}$. From these observations, we suggest that the conductivity in the materials is lowered when the microdomains are large.

A sintering temperature dependence of the intensity of extra reflection and diffuse scattering in SAEDP recorded from $Gd_{0.25}Ce_{0.75}O_{1.875}$ is shown in Fig. 3a. The intensity of extra reflection and diffuse scattering in SAEDP increased with an increase in sintering temperature. Both the extra reflection and diffuse scattering in SAEDP recorded from the specimen sintered at 1,550 °C were much stronger than those in SAEDP recorded from the specimen sintered at 1,000 °C. This indicates that small clusters of oxygen vacancies and associated cations are created at 1,000 °C and the microdomains develop from these clusters when the temperature exceeds 1,000 °C (as illustrated in Fig. 3b).

In Fig. 4, we speculate about the possible mechanism of microdomains formation in the doped CeO_2-sintered bod-

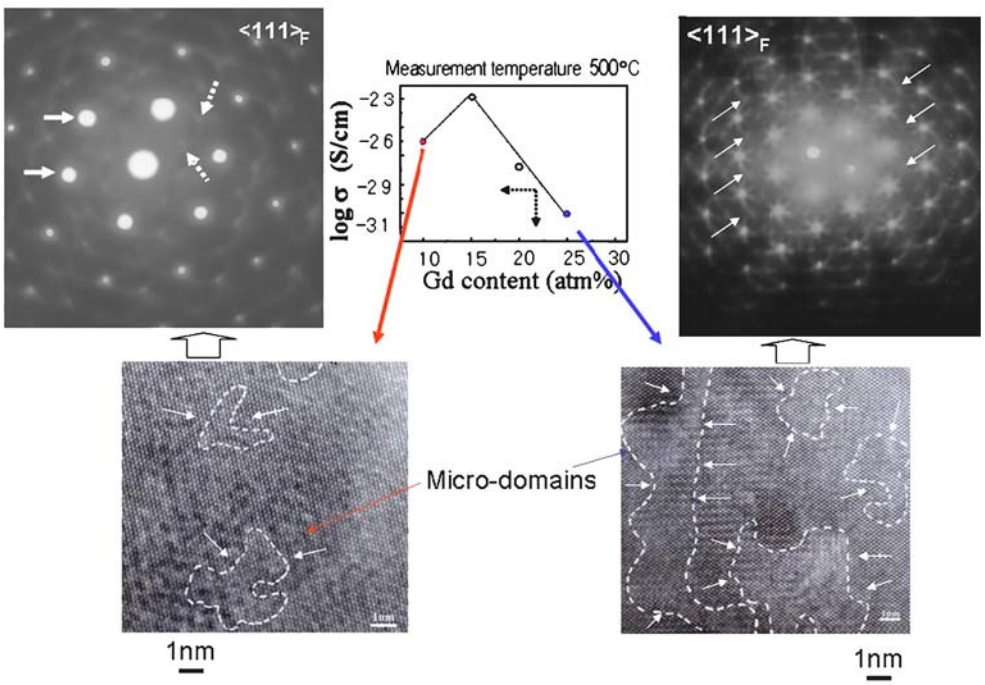

Fig. 2 Relationship between conductivity, selected area electron diffraction patterns $<111>_F$ and high-resolution images from $<111>_F$ recorded from Gd-doped CeO_2 specimens sintered at 1,550 °C

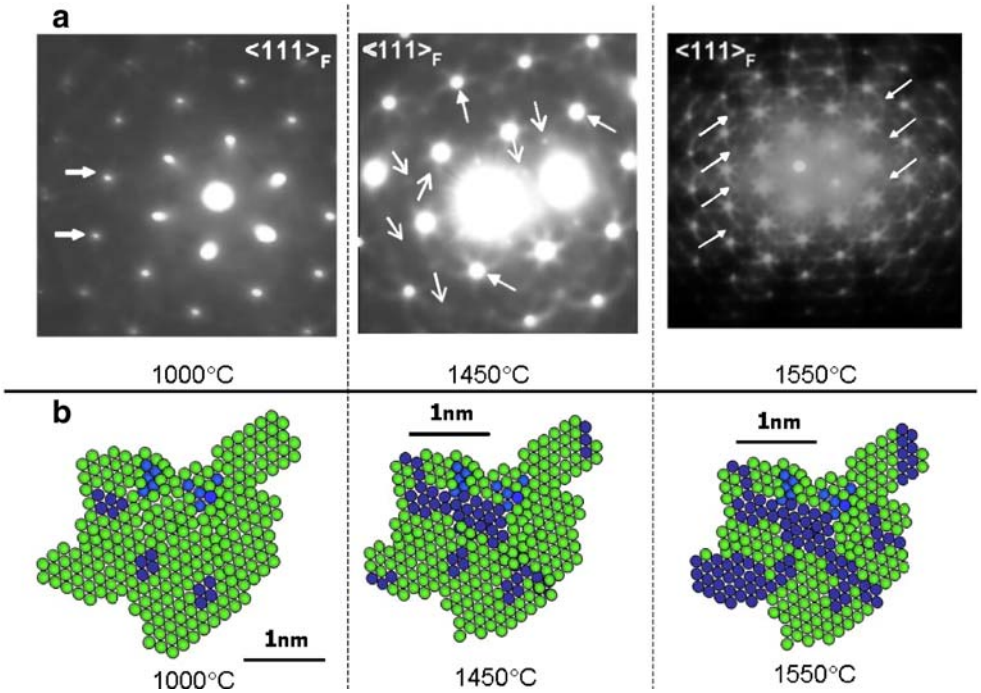

Fig. 3 Sintering temperature dependence of selected area electron diffraction pattern $<111>_F$ recorded from $Gd_{0.25}Ce_{0.75}O_{1.875}$ (**a**) and schematic diagram of sintering temperature dependence of microstructure at atomic scale (**b**)

ies. The grain growth in the specimen sintered at 1,000 °C or lower temperature is homogeneous as shown in Fig. 4a. In the microstructure of specimen sintered above 1,000 °C, a small lattice distortion would be introduced into the grain because of a heterogeneous grain growth. To decrease this lattice distortion, the clusters of oxygen vacancy and cation would be created around the grain boundary area (Fig. 4b). This looks very much like what the space charge layer around a grain boundary in these sorts of material would look like. At high temperature, sintering, the grains heterogeneously grow in the specimens, and this will consequently introduce a large lattice distortion into the

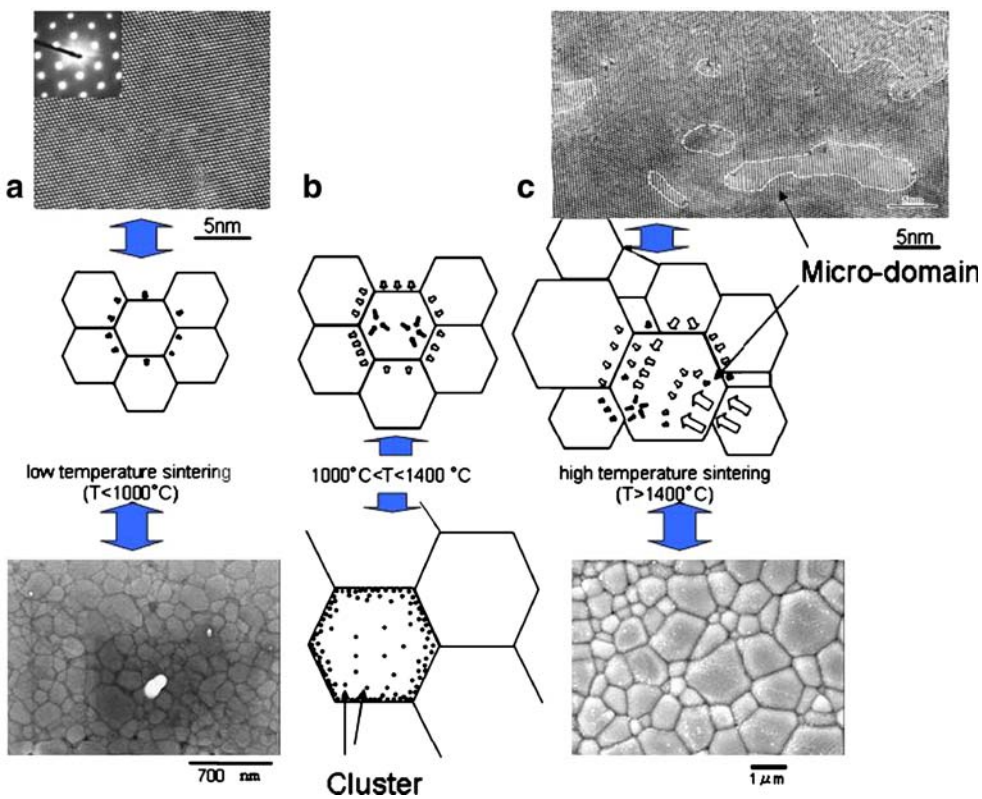

Fig. 4 Speculated mechanism of microdomain formation in doped CeO_2-sintered bodies. Microstructural feature of the specimen sintered at 1,000 °C or lower temperature (**a**), 1,000 to 1,400 °C (**b**), and 1,450 °C or higher temperature (**c**)

grain. To minimize this large lattice distortion, the microdomains with ordered oxygen vacancy would develop from introduced clusters in the grains. This suggests that the goal is to produce homogeneous microstructures at the atomic scale to optimize the development of high-quality solid electrolytes.

Figure 5 presents the average grain size dependence of conductivity (Fig. 5a) and activation energy (Fig. 5b) in the $Gd_xCe_{1-x}O_{x-x/2}$- (x=0.1, 0.15, 0.2, and 0.25) sintered bodies, which were obtained by conventional sintering. The conductivity in the specimens showed the curvature in the grain size dependence of conductivity (Fig. 5a) as is expected. The conductivity decreased with decreasing average grain size and reached the lowest value at an average grain size of between 500 and 1,000 nm. However, contrary to the expected trend, the conductivity is seen to increase slightly when the grain size dips below 500 nm. In addition, the activation energy mirrors this maximum at the same grain size in each composition, indicating that the mobility of oxide ions is the largest at the smaller grain sizes in this $Gd_xCe_{1-x}O_{2-x/2}$ (x=0.1, 0.15, 0.2, and 0.25) system. In the past, this phenomenon was explained by the relative distribution of space charge effects. The space charge region would be confined to the grain boundary interface region. This is a resistive region, so it would follow that as the grain boundary density increased as the grain size reduced, the influence of the space charge layer would increase—giving rise to increased resisitivity. As the grain size got smaller, then, at some point the space charge layers overlap and conductivity would not decrease. If this was simply the explanation, then we would observe a gradual transition in conductivity and activation energy. Instead, we observe changes of conductivity and activation energy, which are quite different in each composition, as shown in Fig. 5a and b. We suggest this is not all attributable to space charge changes and that other microstructural features within the grain are also beginning to have an influence. In the small grain size region, the microstructure of the sintered body is homogeneous as demonstrated in Fig. 4a. At the lowest conductivity region in each composition, a lot of small clusters of ordered oxygen vacancy are created around the grain boundary region (Fig. 4b). In the larger grain size region, the small clusters combine with each other and the microdomains with ordered structure of oxygen vacancy developed within the whole grain (Fig. 4c). We suggest that the conduction pathway now develops inside the specimen at the microdomain interface. Both change of the space charge layer width around the grain boundary and the microdomain structure within the grain would lead to the different tendency of grain size dependence of conductivity in each composition. This is our idea to explain why the grain size dependence of conductivity in each composition is so different.

Comparison of the grain size dependence of conductivity between Gd- and Y-doped CeO_2 is shown in Fig. 6. The authors have reported the grain size dependence of conductivity in $Y_xCe_{1-x}O_{2-x/2}$ (x=0.1, 0.15, 0.2, and 0.25) before [21].The general tendency of grain size dependence of conductivity in the Y-doped CeO_2 system is the same as that in Gd-doped CeO_2 system. However, there are some different and interesting points in the data from the two systems. In both cases, there is a similar curvature in the grain size dependence of conductivity. However, the lower point of the conductivity in the Y-doped CeO_2 system was shifted to the smaller grain size values as shown in Fig. 6b. In addition, the lowering of conductivity in $Y_{0.25}Ce_{0.75}O_{1.875}$ from that in $Y_{0.15}Ce_{0.85}O_{1.925}$ was 0.4 S/cm. On the other hand, the difference of conductivity between $Gd_{0.25}Ce_{0.75}O_{1.875}$ and $Gd_{0.15}Ce_{0.85}O_{1.925}$ was 0.8 S/cm (Fig. 5). The degradation of conductivity of the Gd-doped CeO_2 system was much larger than that of the Y-doped CeO_2 system (Fig. 6b).

Further interpretation of our data is explained through our microanalysis results. The authors observed the degree of oxygen vacancy ordering in the microdomain using EELS in our previous work [29]. Our microanalysis indicated that the degree of oxygen vacancy in the microdomains associated with $Gd_{0.25}Ce_{0.75}O_{1.875}$ and Sm-doped CeO_2 was much higher than that observed in the micro-

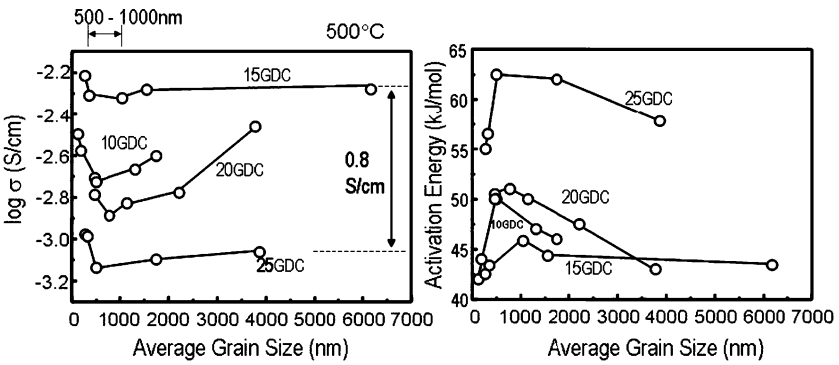

Fig. 5 Average grain size dependence of conductivity (**a**) and activation energy (**b**) of Gd-doped CeO_2-sintered bodies. *10GDC*, $Gd_{0.1}Ce_{0.9}O_{1.95}$; *15GDC*, $Gd_{0.15}Ce_{0.85}O_{1.925}$; *20GDC*, $Gd_{0.2}Ce_{0.8}O_{1.9}$; *25GDC*, $Gd_{0.25}Ce_{0.75}O_{1.875}$. Measurement temperature of conductivity=500 °C

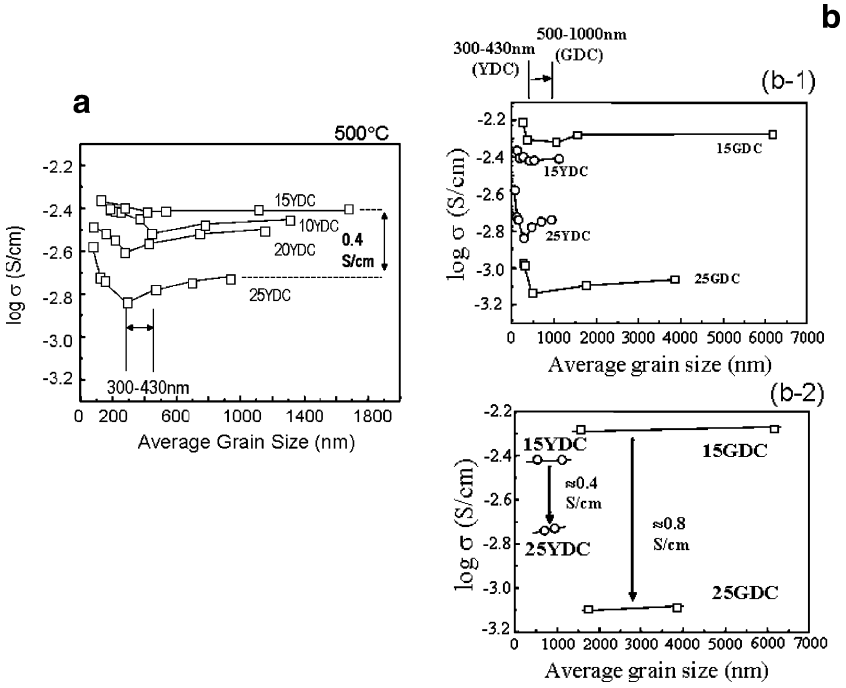

Fig. 6 **a** Average grain size dependence of conductivity of Y-doped CeO_2-sintered bodies. *10YDC*, $Y_{0.1}Ce_{0.9}O_{1.95}$; *15YDC*, $Y_{0.15}Ce_{0.85}O_{1.925}$; *20YDC*, $Y_{0.2}Ce_{0.8}O_{1.9}$; *25YDC*, $Y_{0.25}Ce_{0.75}O_{1.875}$. **b** Schematic diagram about the different features of grain size dependence of conductivity between Gd- and Y-doped CeO_2. Measurement temperature of conductivity=500 °C

domains formed in Y- and Dy-doped CeO_2. The oxygen vacancy ordering in the microdomain depends on the dopant type in a sequence of Gd>Sm>Dy>Y>Yb, which can be explained by a concept of lattice constant misfit between CeO_2 and the C-type dopant oxide structure M_2O_3 (M=Gd, Sm, Dy, Y, and Yb), as shown in Fig. 7. In the case of the Y-doped CeO_2 system, the cluster of oxygen vacancy and Y cation in Y-doped CeO_2 would be easily formed around the grain boundary area to reduce induced lattice distortion at a lower sintering temperature as compared with the Gd-doped CeO_2 system. Because the average grain size of sintered bodies is changed by the sintering temperature of the conventional sintering process, the aforementioned saddle point of the conductivity observed in the Y-doped CeO_2 system would be shifted to a smaller grain size region. When the dopant content is 15 atm%, the amount and size of the microdomain in doped CeO_2-sintered bodies are too small to impact the conductivity in the specimens. Consequently, the change of grain size dependence of conductivity in $Gd_{0.15}Ce_{0.85}O_{1.925}$ and $Y_{0.15}Ce_{0.85}O_{1.925}$ was not large as shown in Figs. 5a and 6a. The domain size and content increased with an increase in

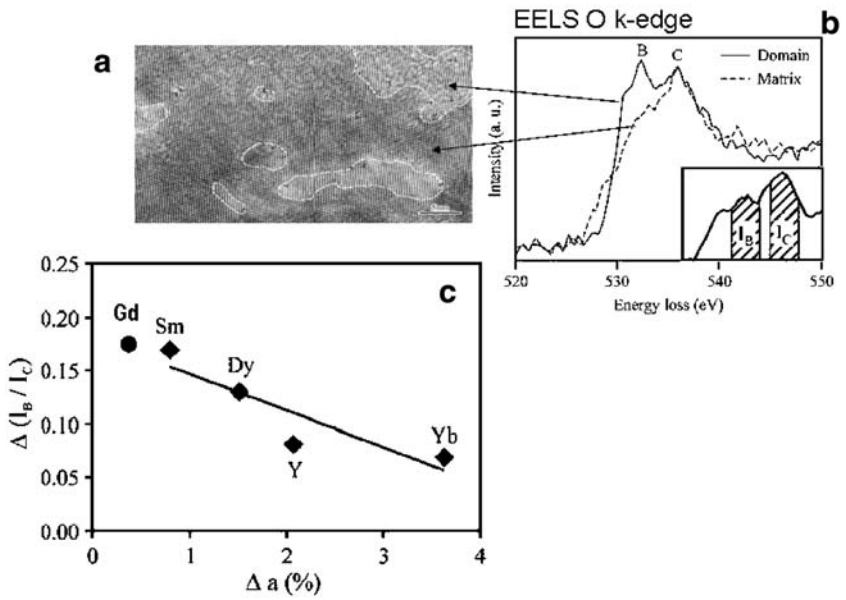

Fig 7 High-resolution image (**a**), EELS spectra (**b**), and dopant-type dependence of degree of oxygen vacancy ordering in the microdomain (**c**) of $M_{0.25}Ce_{0.75}O_{1.875}$ (M: Gd, Sm, Dy, Y, and Yb) sintered bodies

doping concentration to 25 atm%. The development of microdomains with a higher degree of ordering of oxygen vacancy would lead to a more conspicuous decrease in oxide ionic conductivity of doped CeO_2.

As discussed in Figs. 5 and 6, the clusters of oxygen vacancy and cation would make the conductivity a minimum in the grain size dependence of conductivity. Some of the clusters would be combined around the grain boundaries. We suggest that the microdomains with ordered structure of oxygen vacancy develop from these bundles of clusters. After the microdomain is fully grown in the microstructure, it is not so easy to maximize the conductivity in doped CeO_2. Effectively, the limits of microdomain formation will depend on the composition. Therefore, to optimize the microstructure of doped CeO_2, it is the small grain size region that we must concentrate on. To demonstrate this challenge, we selected Dy-doped CeO_2 as an example of doped CeO_2, which we can control. So far, nobody was interested in the Dy-doped CeO_2 as a high-quality solid electrolyte because of its reported low conducting property. However, using our approach, it should be possible to maximize the conductivity by optimizing the microstructure. To optimize the microstructure of $Dy_{0.2}Ce_{0.8}O_{1.9}$, we fabricated the dense sintered body using the PECS process. This method is useful for fabrication of the homogeneous microstructure of doped CeO_2. The conductivity in PECS $Dy_{0.2}Ce_{0.8}O_{1.9}$ and CS $Dy_{0.2}Ce_{0.8}O_{1.9}$ are presented in Fig. 8a. The conductivity in PECS $Dy_{0.2}Ce_{0.8}O_{1.9}$ is the same level as that in CS $Gd_{0.1}Ce_{0.9}O_{1.95}$ and CS $Gd_{0.2}Ce_{0.8}O_{1.9}$, while the conductivity in CS $Dy_{0.2}Ce_{0.8}O_{1.9}$ is much lower than that in Gd-doped CeO_2. As shown in Fig. 8b and c, the microdomain in the homogeneous microstructure of PECS $Dy_{0.2}Ce_{0.8}O_{1.9}$ was just visible. This indicates that we have a chance to design the microstructure in doped CeO_2 by the processing route design, in which case it should be done before microdomains develop in the specimen by high-temperature sintering.

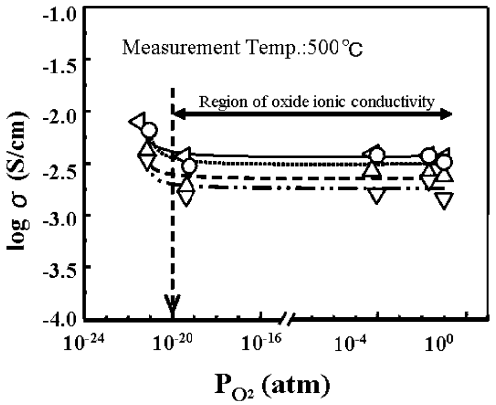

Fig. 9 Partial oxygen pressure dependence of conductivity of (PECS+CS) Dy-doped CeO_2-sintered bodies: *triangles pointing left*, $Dy_{0.15}Ce_{0.85}O_{1.925}$ (average grain size=340 nm); *circles*, $Dy_{0.2}Ce_{0.8}O_{1.9}$ (average grain size=345 nm); *upright triangles*, $Dy_{0.2}Ce_{0.8}O_{1.9}$ (average grain size=153 nm); *inverted triangles*, $Dy_{0.25}Ce_{0.75}O_{1.875}$ (average grain size=273 nm). Measurement temperature=500 °C

To conclude the conduction mechanism in PECS $Dy_{0.2}Ce_{0.8}O_{1.9}$, the relationship between partial oxygen pressure and conductivity in $Dy_{0.2}Ce_{0.8}O_{1.9}$ is demonstrated in Fig. 9. The conductivity in PECS $Dy_xCe_{1-x}O_{2-x/2}$ (x=

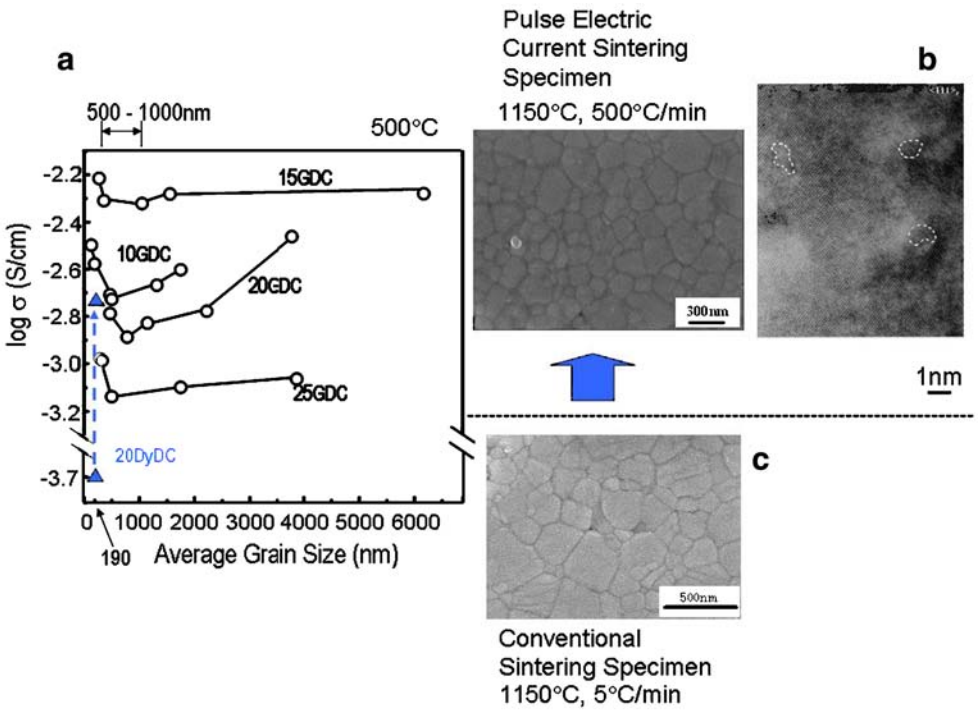

Fig. 8 Comparison of conductivity among $Dy_{0.2}Ce_{0.8}O_{1.9}$ and $Gd_xCe_{1-x}O_{2-x/2}$ specimens (x=0.1 0.15, 0.2, and 0.25) (**a**), microstructural features of (PECS+CS) $Dy_{0.2}Ce_{0.8}O_{1.9}$ (**b**), and CS $Dy_{0.2}Ce_{0.8}O_{1.9}$ specimens (**c**)

0.15, 0.2, and 0.25) was constant from 1 to 10^{-21} atm at 500 °C. Accordingly, it is concluded that the improvement of conductivity in PECS $Dy_{0.2}Ce_{0.8}O_{1.9}$ is attributable to the enhancement of oxide ionic conductivity because of the optimization of the microstructure at the atomic scale in doped CeO_2. Based on those results, we expect that the conductivity in $Gd_{0.2}Ce_{0.8}O_{1.9}$ and $Gd_{0.25}Ce_{0.75}O_{1.875}$ will be maximized using the present idea for optimization of the microstructure.

Summary

The influence of microstructural features on conducting property in CeO_2 doped with Gd, Y, and Dy was examined to propose the concept for a design of nanostructured doped CeO_2 solid electrolytes for IT-SOFC application. To design the microstructure at atomic scale, round-shaped doped CeO_2 powders were prepared using the carbonate coprecipitation method. Dense sintered bodies (more than 95% of theoretical density) were obtained using CS or a combined process of the PECS and CS methods. The specimen obtained by high-temperature CS of more than 1,450 °C had a large number of big microdomains with an ordered structure of oxygen vacancy. The grain size dependence of conductivity in the specimen was influenced by this heterogeneous microdomain structure in doped CeO_2. Because it can be concluded that we have a chance to design the microstructure in doped CeO_2 before the microdomain develops in the specimen by high-temperature sintering, the (PECS+CS) $Dy_{0.2}Ce_{0.8}O_{1.9}$ with a homogeneous microstructure was fabricated at the region of small grain size. The conductivity in PECS Dy-doped CeO_2 became comparable to the conductivity in CS $Gd_{0.1}Ce_{0.9}O_{1.95}$ and CS $Gd_{0.2}Ce_{0.8}O_{1.9}$, while the conductivity in CS $Dy_{0.2}Ce_{0.8}O_{1.9}$ is much lower than that in CS Gd-doped CeO_2. Accordingly, it is concluded that the nanoheterostructure can be optimized by processing route design. This optimization of the microstructure should be performed before the microdomain develops in the specimens sintered at high temperature. We believe that we have a chance to design the optimum microstructure using a combination of an ultimate analysis of the microstructure and processing route design for a development of high-quality doped CeO_2 soild electrolytes in IT-SOFCs.

References

1. Fergus JW (2007) Sens Actuators B Chem 121(2):652
2. Izu N, Shin W, Matsubara I, Murayama N (2004) Sens Actuators B Chem 101(3):381
3. Yamazoe N, Miura N (1999) MRS Bull 24(6):37
4. Arico AS, Sin A, Kopnin E, Dubitsky Y, Zaopo A, La Rosa D, Gullo LR, Antonucci V (2007) J Power Sources 164(1):300
5. Riess I (2005) Solid State Ion 176(19–22):1667
6. Hamakawa S, Hayakawa T, York APE, Tsunoda T, Yoon YS, Suzuki K, Shimizu M, Takehira K (1996) J Electrochem Soc 143 (4):1264
7. Patil BB, Pawar SH (2007) Appl Surf Sci 253(11):4994
8. Goodenough JB (2003) Oxide-ion electrolytes. In: Kreuer KD, Clarke DR, Ruhle M, Bravman JC (eds) Annu Rev Mater Res 33:91–128
9. Steel BCH (2001) Nature 414(15):345
10. Rupp JLM, Gauckler LJ (2006) Solid State Ion 177(26–32):2513
11. Reddy KR, Karan K (2005) J Electroceramics 15(1):45
12. Gourba E, Ringuede A, Cassir M, Billard A, Paivasaari J, Niinisto J, Putkonen M, Niinisto L (2003) Ionics 9(1–2):15
13. Nesaraj AS, Raj IA, Pattabiraman R (2007) Indian J Chem Technol 14(2):154
14. Yanhong Y, Shaoyu L, Changrong X, Guangyao M (2007) J Power Sources 167(1):90
15. Barnett SA, Zhongliang Z (2006) J Power Sources 157(1):422
16. Mori T, Drennan J, Wang Y, Li JG, Ikegami T (2002) J Therm Anal Calorim 70:309
17. Mori T, Drennan J, Lee JH, Li JG, Ikegami T (2002) Solid State Ionics 154–155:461
18. Mori T, Wang Y, Drennan J, Auchterlonie G, Li JG, Ikegami T (2004) Solid State Ionics 175:641
19. Mori T, Drennan J, Wang Y, Lee JH, Li JG, Ikegami T (2003) J Electrochem Soc 15(6):A665
20. Mori T, Drennan J, Wang Y, Auchterlonie G, Li JG, Yago A (2003) Sci Technol Adv Mater 4:213
21. Ou DR, Mori T, Ye F, Takahashi M, Zou J, Drennan J (2006) Acta Mater 54(14):3737
22. Ou DR, Mori T, Ye F, Zou J, Drennan J (2007) Electrochem Solid-State Lett 10(1):1
23. Mori T, Kobayashi T, Wang Y, Drennan J, Nishimura T (2005) J Am Ceram Soc 88(7):1981
24. Mori T, Drennan J, Wang Y, Auchterlonie G, Li JG (2004) J Ceram Soc Jpn 112(5):S642
25. Ye F, Mori T, Ou DR, Takahashi M, Zou J, Drennan J (2007) J Electrochem Soc 154(2):B180
26. Ye F, Mori T, Ou DR (2007) J Nanosci Nanotechnol 7:1
27. Ye F, Mori T, Ou DR, Zou J, Drennan J (2007) Mater Res Bull 42:943
28. Ye F, Mori T, Ou DR, Zou J, Auchterlonie G, Drennan J (2007) J Appl Phys 101:113528–113531
29. Ou DR, Mori T, Ye F, Kobayashi T, Zou J, Auchterlonie G, Drennan J (2006) Appl Phys Lett 89(17):1911
30. Mendelson MI (1969) J Am Ceram Soc 52(8):443
31. Soldatov AV, Ivanchenko TS, Della LS, Kotani A, Iwamoto Y, Bianconi A (1994) Phys Rev B 50:5074